Hirvonen, Petri; La Boissonière, Gabriel Martine; Fan, Zheyong; Achim, Cristian; Provatas, Nikolas; Elder, Ken R.; Ala-Nissilä, Tapio

Grain extraction and microstructural analysis method for two-dimensional poly and quasicrystalline solids

Please cite the original version:
Hirvonen, P., La Boissonière, G. M., Fan, Z., Achim, C., Provatas, N., Elder, K. R., & Ala-Nissilä, T. (2018). Grain extraction and microstructural analysis method for two-dimensional poly and quasicrystalline solids. *Physical Review Materials*, 2(10), 1-14. Article 103603. https://doi.org/10.1103/PhysRevMaterials.2.103603

Grain extraction and microstructural analysis method for two-dimensional poly and quasicrystalline solids

Petri Hirvonen[*]

QTF Centre of Excellence, Department of Applied Physics, Aalto University School of Science, P.O. Box 11000, FIN-00076, Aalto, Espoo, Finland

Gabriel Martine La Boissonière

Department of Mathematics and Statistics, McGill University, Montreal, QC H3A 0B9, Canada

Zheyong Fan

QTF Centre of Excellence, Department of Applied Physics, Aalto University School of Science, P.O. Box 11000, FIN-00076, Aalto, Espoo, Finland

Cristian Vasile Achim

Water Research Center for Agriculture and Mining (CRHIAM), University of Concepción, 4030000 Concepción, Chile

Nikolas Provatas

Department of Physics and Centre for the Physics of Materials, McGill University, Montreal, QC H3A 0B9, Canada

Ken R. Elder

Department of Physics, Oakland University, Rochester, MI 48309, USA

Tapio Ala-Nissila

QTF Centre of Excellence, Department of Applied Physics, Aalto University School of Science, P.O. Box 11000, FIN-00076, Aalto, Espoo, Finland
and Interdisciplinary Centre for Mathematical Modelling and Department of Mathematical Sciences, Loughborough University, Loughborough, Leicestershire LE11 3TU, United Kingdom

While the microscopic structure of defected solid crystalline materials has significant impact on their physical properties, efficient and accurate determination of a given polycrystalline microstructure remains a challenge. In this paper, we present a highly generalizable and reliable variational method to achieve this goal for two-dimensional crystalline and quasicrystalline materials. The method is benchmarked and optimized successfully using a variety of large-scale systems of defected solids, including periodic structures and quasicrystalline symmetries to quantify their microstructural characteristics, e.g., grain size and lattice misorientation distributions. We find that many microstructural properties show universal features independent of the underlying symmetries.

I. INTRODUCTION

The properties of matter in its solid, crystalline state are typically dictated not only by the elemental composition and lattice structure but also the microstructure, i.e., the distribution of grains and lattice defects. The microstructure can have a great influence on mechanical [1–3], thermal [4–6], electrical [6,7], and other physical properties of the solid phase [8]. However, mapping the exact relationships between the atomistic details of the microstructure and the more macroscopic material properties is a major challenge—realistic microstructures are often very complicated and even isolated defects such as grain boundaries or triple junctions have a large number of degrees of freedom to be investigated [2,9]. Regardless, realistic model systems and detailed knowledge of the distributions of grains and defects are paramount to this task.

Modeling the formation of realistic microstructures—a prerequisite to investigate the connections between microstructure and material properties—is a formidable challenge due to the complex elastic interactions between defects and the vast range of length and timescales involved. While some progress has been made using traditional atomistic modeling methods such as accelerated molecular dynamics (MD) [10], the recently developed phase-field crystal (PFC) approach is a strong contender. PFC models naturally incorpo-

---

[*]petri.hirvonen@aalto.fi

rate diffusion and elastoplasticity in defected crystalline materials and have been shown to produce realistic microstructures for selected materials [11–13]. Their formulation allows modeling the slow evolution of microstructures with atomic-level resolution in systems of up to mesoscopic size.

Characterizing and analyzing microstructures remains a very difficult task, however. While there exist several methods including variational [14–17] and geometric [18] to detect the lattice orientation in a polycrystalline material, there have only been few attempts to further extract and measure the network of grains as in Ref. [11]. Notably, fully atomistic approaches [13,19] have been developed to solve both problems by first assigning an orientation to atoms based on their local environment and then assigning them to appropriate grains in an iterative fashion.

Another open issue concerns aperiodic crystalline structures. In particular, the microstructures of quasicrystals and their impact on physical properties are not well known. Quasicrystals are a group of materials that show no long-range translational order but display long-range orientational order, which makes structural analysis a major challenge with traditional means. In particular, they can have, for example, five, eight, ten or 12-fold rotational symmetries, which are not possible in regular periodic crystals. First discovered in 1984, quasicrystals are today known to form a family of hundreds of metallic alloys and soft-matter systems. Quasicrystals have many potential applications due to their low coefficient of friction, resistance to oxidation [20], and are also attractive in catalytic [21] and epitaxial [22] applications. Modeling quasicrystals and their evolution using the PFC approach shows great promise. Recent works have considered quasicrystal growth modes [23], interfaces between quasicrystalline grains from multiple separate seeds [24], monolayers on quasicrystalline surfaces [25], and even three-dimensional quasicrystalline systems [26]. On the other hand, where periodic crystals display an endlessly repeating motif quasicrystals do not obey this rule, which drastically complicates both the detection of a lattice orientation and grain extraction with the current methods [11,13,19]. To our knowledge, no attempts toward grain extraction in quasicrystals have been reported.

In this paper, we present and benchmark a powerful variational method for extracting individual grains and analyzing the microstructure in two-dimensional (2D) poly(quasi)crystalline systems from large-scale PFC grain coarsening simulations. We consider both regular square and hexagonal lattice types, as well as quasicrystals with ten and 12-fold rotational symmetries. We study the sizes, aspect ratios, circularities, and neighbor counts of individual grains, as well as the size ratios, misorientations, and misalignments between neighboring grains. We demonstrate that the method can be reliably used to quantify the microstructure of 2D crystals and quasicrystals.

The remainder of this work is organized as follows: Section II A introduces the grain extraction method and Sec. II B describes the present model systems and the PFC model used to characterize them. In Sec. III A, the performance of the grain extraction method is evaluated and in Sec. III B results of microstructural analysis of different (quasi)lattice types are given. Section IV concludes and summarizes our results.

Supplemental Material [27] gives more details of our methods and additional results.

II. METHODS

A. Grain extraction method

The grain extraction method proposed here consists of four steps. In the first step, a density field describing a crystalline or quasicrystalline 2D system is transformed into an "orientation field" indicating the crystallographic or, more simply, the lattice orientation and crystalline order at each point. In this paper, for the sake of concreteness and ease of implementation we consider mainly PFC generated density fields, but virtually any data containing the spatially distributed atomic density is acceptable; see Supplemental Sec. S1 [27] for examples. Next, a "deformation field" is constructed from the orientation field, highlighting the grain boundaries and isolated dislocations. Then, the system is segmented into "subdomains" via level-fill growth in the deformation field. As the final step, some subdomains need to be merged to recover a structure closer to the true network of grains. This subsection describes these steps in detail.

We start with a 2D density field $\psi \equiv \psi(x, y)$, describing a crystalline system as a periodic lattice of density peaks, which can be transformed into a smooth, complex-valued orientation field ϕ whose argument $\arg \phi$ represents the local orientation and whose norm $|\phi|$ indicates the local crystalline order, or lack thereof; namely, defects. The orientation field ϕ is given by

$$\phi = \{[(\psi - \min \psi) * K][\psi - \min \psi]\} * G, \quad (1)$$

and Fig. 1 visualizes some of its different components for a hexagonal crystal and a ten-fold quasicrystal. In Eq. (1), ψ is first shifted so that its global minimum becomes zero. The shifted field is then convolved with a complex-valued kernel K [Figs. 1(a), 1(b), 1(d), and 1(e)], which is described in more detail in the next paragraph. This convolution results in a field whose maxima commensurate with those in ψ display a complex phase corresponding to the local orientation [Figs. 1(c) and 1(f)]. As an aside, it seems ϕ can be constructed equally well by using $\psi * K$ here, but we used $(\psi - \min \psi) * K$ in our numerical implementation. Next, this convolution is multiplied by $\psi - \min \psi$ to mask out the incommensurate maxima and to pick out only the commensurate maxima with the correct orientation [Figs. 1(c) and 1(f)]. Finally, a convolution with a Gaussian kernel just wide enough to filter out the atomic-level structure is applied. More specifically, for our PFC systems, we found the kernel widths $\sigma_G = 0.15$ and $\sigma_G = 0.05$ in Fourier space ($k = 1$ corresponds to the first set of peaks in their Fourier spectra) sufficient for the periodic and quasilattices, respectively. The method is not very sensitive to σ_G as long as the resulting ϕ is smooth on atomic length scales (a prerequisite for the subsequent steps of the algorithm). Excessive smoothing leads to loss of resolution, of course.

The complex-valued, annular kernel K is given in Fourier space [Figs. 1(b) and 1(e)] by

$$K(\mathbf{k}) = \exp\left[-(|\mathbf{k}| - q)^2/(2\sigma_K^2) + i\, m \arg(\mathbf{k})\right], \quad (2)$$

where $\mathbf{k} = (k_x, k_y)$, q and σ_K are the major and minor radii, respectively, i is the imaginary unit and m is the order of
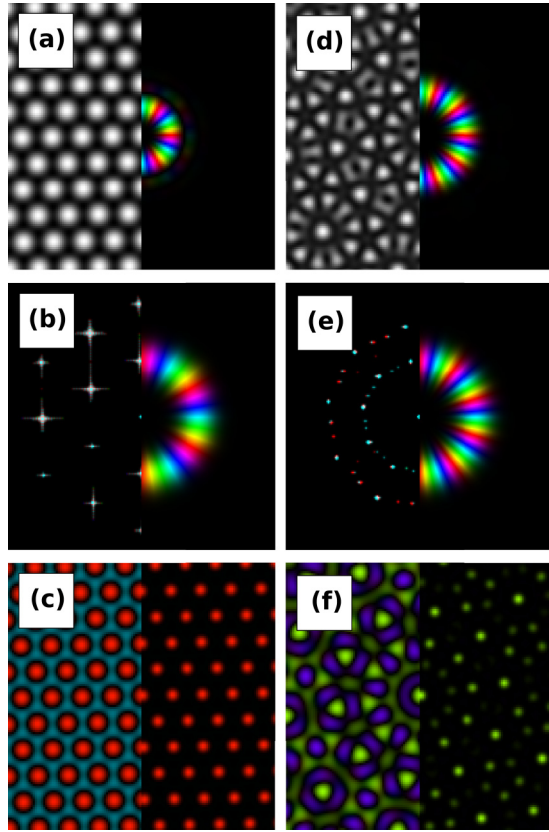
FIG. 1. Different components of Eq. (1). Amplitude is mapped to brightness and phase to hue (real-valued fields are shown in gray scale). The left column is for a hexagonal crystal and the right column for a ten-fold quasicrystal. Panels (a) and (d) juxtapose the density field $\psi(x, y)$ (left half) with the kernel $K(x, y)$ (right half) in direct space, whereas panels (b) and (e) show them in Fourier space. Some image processing has been applied to the left half of (b) and (e) to make the spectral peaks stand out better. Panels (c) and (f) contrast the convolution $(\psi - \min \psi) * K$ (left half) with the product $[(\psi - \min \psi) * K][\psi - \min \psi]$ (right half) which masks out the incommensurate maxima and picks out only the commensurate maxima with the correct orientation.

rotational symmetry. The kernel's major radius q is chosen to match a characteristic length scale in ψ (we used $q = 1$ to match the lattice constant) and its phase must have the same order of rotational symmetry m as ψ, e.g., $m = 6$ for a hexagonal system. The minor radius σ_K should be narrow enough to avoid significant contribution from other, potentially interfering modes ($\sigma_K = 0.2$ appears to work in all the cases here). The method is not very sensitive to q and σ_K as long as the desired length scale is selected predominantly. This is due to the Gaussian convolution applied that washes out the fine details. In direct space, the kernel overlaps with the m neighbors of the m-fold symmetric maxima in ψ and has the same m-fold symmetry [Figs. 1(a) and 1(d)]. Due to these two properties and the fact that (quasi)crystals have long-range orientational order, all m neighbors of all m-fold symmetric maxima contribute the same complex phase in the convolution $(\psi - \min \psi) * K$ within a single grain. The commensurate maxima in $(\psi - \min \psi) * K$ display this complex phase which indicates the neighbor orientations in

ψ [Figs. 1(c) and 1(f)]. Note that this phase $0 \leqslant \arg \phi \leqslant 2\pi$ and has to be scaled by $1/m$ to recover the actual lattice orientation.

As an aside, it appears possible to form ϕ for various even-fold (2, 4, 6, 8,...) symmetric (quasi)lattices. Odd-fold (5, 7,...) quasilattices display double-, i.e., even-fold, symmetry centers whose degeneracy leads to an ill-defined complex phase where $\phi = 0$. As a second aside, as with other similar methods, it is not trivial to extend ϕ to 3D. The complex-valued, annular kernel could perhaps be replaced with a spherical three-vector shell. However, while in 2D there is a unique rotation axis about which the spectrum of ψ is symmetric, in 3D there are several—possibly more than the three sufficient to rotate a 3D (quasi)crystal—and, depending on the lattice type, they might not share the same m. Constructing the kernel then becomes a very unintuitive task in general, but could be possible for specific simpler lattices such as cubic ones. All in all, addressing these extended problems goes well beyond the scope of this work.

Grains are regions of uniform lattice orientation. Due to the discrete nature of (quasi)lattices, where two grains meet continuous deformation and structural defects accommodate the orientational mismatch. We exploit the fact that grains are enclosed by such imperfections in extracting grains. The orientation field retains such features which can be mapped by the magnitude of its gradient

$$|\nabla \phi| = \sqrt{\Re(\phi_x)^2 + \Im(\phi_x)^2 + \Re(\phi_y)^2 + \Im(\phi_y)^2}, \quad (3)$$

where $\Re$ and $\Im$ give the real and imaginary parts, respectively, while ϕ_x and ϕ_y denote the partial derivatives of ϕ with respect to the x and y directions. From $|\nabla \phi|$, one can construct a filtered, smooth deformation field χ that is more compatible (explained in the next paragraph) with the two final steps of the grain extraction algorithm. The deformation field is given by

$$\chi = \sum_{n=0}^{2^n a < \min(W, H)/2} \frac{|\nabla \phi|^p * \exp[-|\mathbf{r}|^2/(2 \cdot 2^{2n} a^2)]}{\max\{|\nabla \phi|^p * \exp[-|\mathbf{r}|^2/(2 \cdot 2^{2n} a^2)]\}}, \tag{4}$$

where a is the lattice constant, W and H are the dimensions of the system, and p is a tunable exponent. Equation (4) gives a sum of normalized convolutions between a power of the gradient and Gaussian kernels of width 2^n lattice constants. The sum is truncated before the kernel width reaches the smaller of the system dimensions. Figure 2 demonstrates ϕ and χ for polycrystalline systems of hexagonal and 12-fold quasicrystalline lattice types. Grain boundaries and individual defects appear in $|\nabla \phi|$ as regions of higher values and exponent p can be used either to boost ($p > 1$) or to attenuate ($p < 1$) them. The effect of p on the final segmented grain structure and its values found suitable for the lattice types considered here are discussed in Sec. III A 2.

With the help of χ, a polycrystalline system can be segmented into subdomains. Each local minimum in χ is treated as a seed and the subdomains are grown from these seeds by climbing the χ value landscape. All growth fronts climb χ at the same rate and stop when the subdomains collide. The lattice orientation of a subdomain is given by the average of ϕ over it. This procedure is illustrated by the time series in
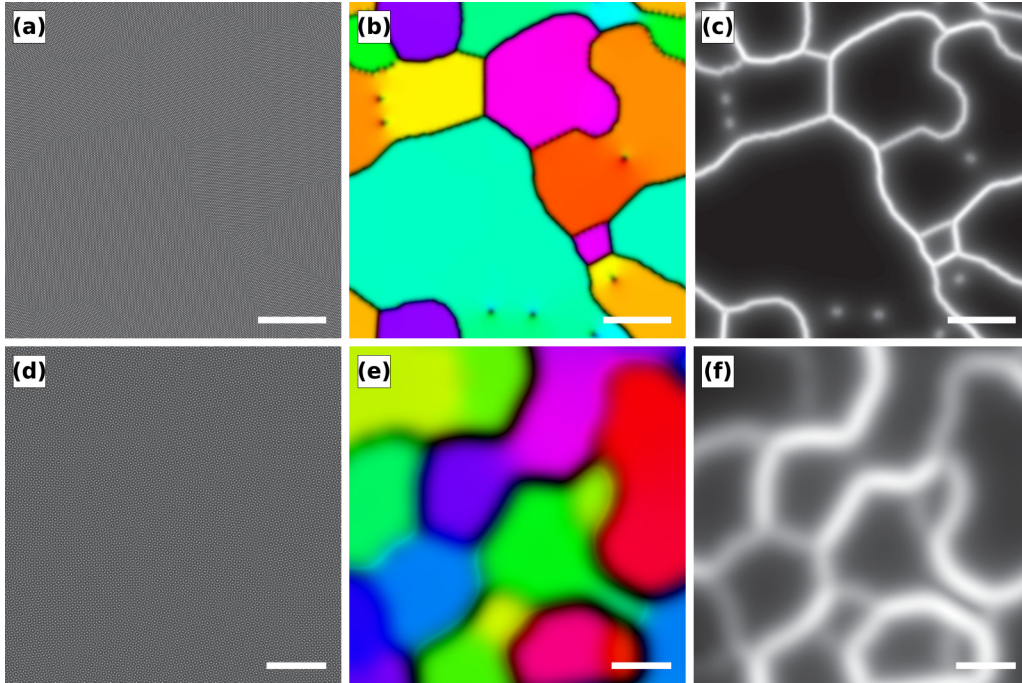
FIG. 2. Polycrystalline hexagonal (top panels) and 12-fold quasicrystal (bottom panels) from the PFC model. In (a) and (d), we show the density field ψ, in (b) and (e), the orientation field ϕ, and in (c) and (f), the deformation field χ. The scale bars have lengths $40a_{\text{hex}}$ and $20a_{\text{hex}}$ for the hexagonal and the 12-fold systems, respectively.

Fig. 3. We considered using $|\Delta\phi|^p$ directly as the deformation field in lieu of χ, but the former has a large number of local minima each corresponding to a subdomain whose number exceeds greatly the number of real grains. This additional complexity is likely to lead to a failure in recovering the grain structure in the fourth and final step of the algorithm. Filtering $|\Delta\phi|^p$ further using a single Gaussian kernel is also not ideal, as there is a trade-off between getting rid of the aforementioned excess local minima and smoothing out small-scale features of the microstructure. The formulation given by Eq. (4) filters out most unnecessary local minima without sacrificing much of the small-scale features such as isolated dislocations and kinks of grain boundaries.
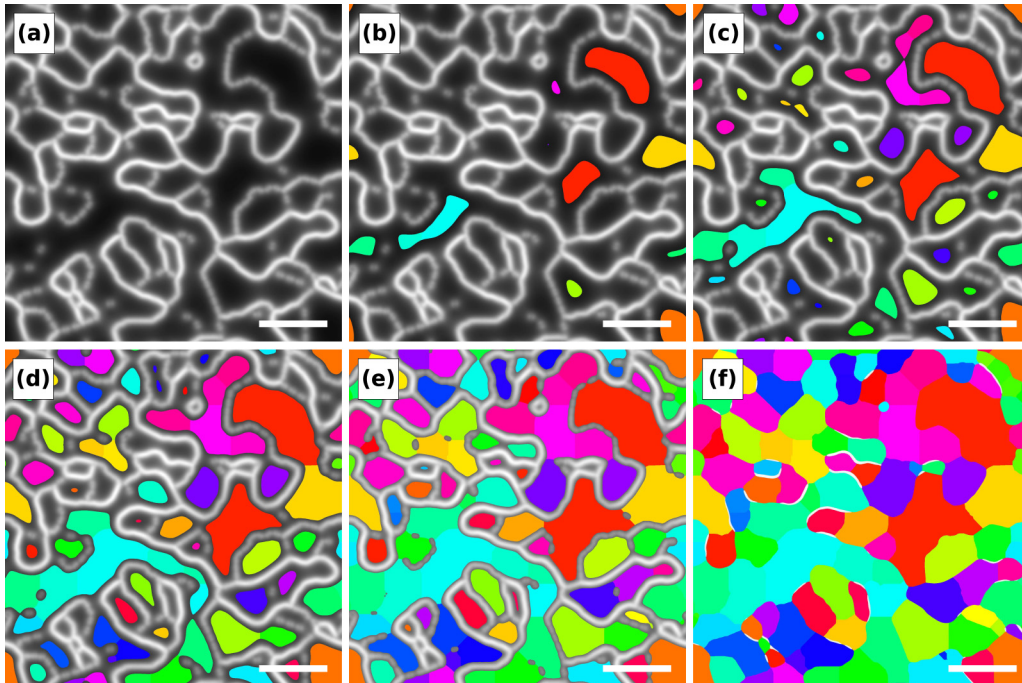

FIG. 3. Time series of subdomain growth in χ. The panels (a)–(f) show snapshots of the growth procedure. The scale bars have length $40a_{\text{hex}}$.

As mentioned above, some grains may host multiple local minima of χ and are consequently subdivided into multiple subdomains. As a final step of the grain extraction algorithm, some neighboring subdomains are merged to recover the true grain structure. Various criteria for merging were considered, but because the subdomains to be merged typically have very similar lattice orientations, a simple misorientation-based criterion was found to be sufficient: merge neighboring subdomains if the relative difference between the two lattice orientations $\theta < \theta^*$. The optimal choice of θ^* for each lattice type is discussed in Sec. III A 2. An additional condition was introduced for very small grains below a certain linear size: such grains are merged with the neighbor that is closest in lattice orientation. As the limit, a linear size of five times the lattice constant was used. Such grains are just barely larger than the dislocations enclosing them. All lattice types considered in this work display roughly similar length scales whereby the approximate dimensionless lattice constant for the hexagonal lattice $a_{\mathrm{hex}} = 4\pi/\sqrt{3} \approx 7.3$ was used for all of them.

Regarding the computational cost of the method, its two bottlenecks are computing the deformation field χ and the subdomain growth step. We implemented the several convolutions in the former using parallelized fast Fourier transforms. The latter was realized as a serial iterative algorithm due to its complexity. We expect that the latter step can be sped up significantly by using an improved, parallelized algorithm. It takes on the order of a few minutes for a quad-core desktop PC to fully process a system of 8192×8192 grid points. The computational performance of the method is discussed in more detail in Supplemental Sec. S2 [27].

B. Model systems

We applied the grain extraction method to study the microstructure and its evolution in polycrystalline systems of different lattice types. We considered regular square and hexagonal lattices, as well as ten and 12-fold quasicrystalline ones. Random polycrystalline 2D systems were obtained from large-scale grain coarsening simulations carried out using a phase field crystal (PFC) model. While conventional atomistic methods such as quantum-mechanical density functional theory and MD have limitations related to the length and timescales available to them, PFC models display multiscale characteristics that render them ideal for modeling realistic microstructures and their formation. The main advantage of PFC models is the access to long, diffusive timescales over which microstructure evolution takes place. Furthermore, due to their numerically convenient nature, mesoscopic systems can be handled readily with atomic-level resolution.

PFC models are a family of continuum methods for structural and elastoplastic modeling of crystalline matter at the atomistic scale. Systems modeled using PFC are described in terms of smooth, classical density fields ψ. Given an initial guess $\psi(t = 0)$, the system's evolution is governed by minimization of its free energy. The free energy is typically given by a simple functional $F(\psi)$ incorporating a double-well potential with gradient terms enabling periodic, i.e., crystalline, solutions for ψ. [28–30]. We chose the simplest PFC model capable of producing the aforementioned four, six, ten and 12-fold (quasi)crystal symmetries. The free-energy

TABLE I. Model parameters and average densities used for the four different lattice types considered in this work. The first column, titled m, indicates the lattice types by their rotational symmetry.

m	R	N	q_1	q_2	$\bar{\psi}$
4	-0.18	2	1	$\sqrt{2}$	-0.28
6	-0.18	1	1	–	-0.25
10	-0.07	2	1	$2\cos(\pi/5)$	-0.161060
12	-0.25	2	1	$2\cos(\pi/12)$	-0.314904

functional of this two-mode model is given by [23,31]

$$ F = \int d\boldsymbol{r} \left(\frac{\psi}{2} \left(R + \prod_{n=1}^{N} \left(q_n^2 + \nabla^2 \right)^2 \right) \psi + \frac{\psi^4}{4} \right). \quad (5) $$

Here, R is related to temperature: if R is positive (above melting), the double-well potential $R\psi^2/2 + \psi^4/4$ favors a uniform (liquid) state with $\psi = 0$, but, if it is negative (below melting), nonzero densities minimize it. Together with the nonzero densities preferred, the term $\psi(\prod_{n=1}^{N}(q_n^2 + \nabla^2)^2)\psi/2$ gives rise to periodic solutions and to elastic behavior by penalizing deviations from the $N = 1$ or 2 length scales controlled by the wave numbers q_n. We minimized the free energy and evolved ψ forward in time assuming diffusive dynamics as

$$ \frac{\partial \psi}{\partial t} = \nabla^2 \frac{\delta F}{\delta \psi}, \quad (6) $$

where $\delta/\delta\psi$ indicates a functional derivative with respect to ψ. Diffusive dynamics strictly conserve the average density $\bar{\psi}$ which, together with R and q_n, controls the symmetries in the periodic ψ, or in other words, the lattice type of the system. Related phase diagrams indicating the equilibrium phase as a function of $\bar{\psi}$, R and q_n can be found in Refs. [11,23]. We adopted $\bar{\psi}$, R and q_n for the hexagonal lattice and the quasicrystals from these works, whereas for the square lattice they were found by trial and error. The parameters $\bar{\psi}$, R, and q_n used for the four different lattice types considered in this work are given in Table I. We used the semi-implicit spectral method given in Ref. [30] although similar spectral methods have been used elsewhere in the literature, for example Ref. [32] used by Refs. [11,13]. The specific numerical method and parameters do not appreciably influence the grain extraction algorithm since the precise atomic behavior is washed out in computing the orientation field. Note that periodic boundary conditions ensue from the use of a spectral method.

For the original PFC model with $N = 1$, for parameters where the hexagonal phase has the lowest energy, the liquid phase is always linearly unstable with respect to small deformations [33]. Consequently, to grow a polycrystalline configuration from a liquid initial state, for most parameter choices it is sufficient to start with a random density field. However, for the quasicrystal systems modeled using Eq. (5) with $N = 2$ and the parameters given in Table I, the liquid is linearly stable to small perturbations. The critical size of initial seeds for stable growth is relatively large for the present quasilattices with the model parameters and the average densities chosen [23,24]. Stability of the quasicrystalline phases
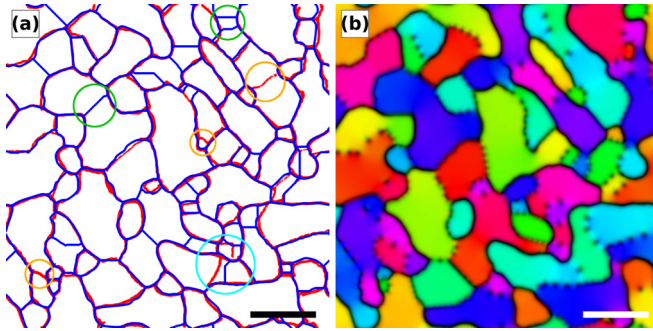
FIG. 4. (a) A comparison between the grains determined by a visual inspection (red) and the subdomains produced by the present method (blue) for a hexagonal system. The green, cyan, and orange circles indicate subdomain borders, minor differences in grain boundary delineation, and inconsistencies, respectively. (b) The corresponding orientation field ϕ. The scale bars have length $40a_{\text{hex}}$. See text for details.

was ensured by exploiting initial states with moderate-sized square tiles of the lattice type desired in random orientations. Tilings of 128×128 and 64×64 tiles were used for the periodic and the quasilattices, respectively. All initial lattice structures were obtained with one-mode approximations, i.e., by summing plane waves [25].

The method was also tested on MD-generated data of free-standing polycrystalline monolayer graphene to investigate the impact of thermal fluctuations—giving rise to displacements of atoms and to out-of-plane buckling of the sheet—on the performance of the method. First, relaxed PFC density fields for polycrystalline graphene were converted into sets of atomic coordinates. The approx. 48×48 nm^2 systems were thermalized at both 1 K and 300 K using a GPUMD code [34,35] with the Tersoff potential [36,37]. Here, we reused systems from our previous work on thermal transport in polycrystalline graphene [4] and the details of the PFC and MD simulations can be found there in full. The relaxed MD coordinates were converted back into 2D density fields suitable for the present grain extraction code by first projecting them onto the xy plane and smoothing atoms with Gaussian peaks.

III. RESULTS

A. Assessment of the grain extraction method

This subsection is dedicated to the assessment of the performance of the grain extraction method and to its optimization to reproduce the hand segmentations of the authors of the patched network of grains in a polycrystalline system. The preliminary networks of subdomains are first investigated, before optimizing subdomain merging step to match human judgment. Lastly, the method's applicability to MD data is demonstrated.

1. Assessment of the subdomain network

A prerequisite for capturing the correct grain structure is a patchwork of subdomains that captures the outlines of the grains. Figure 4 demonstrates in red color the grain boundaries in a polycrystalline system as determined by one of the

authors here (K.R.E.) by a simple visual examination of the atomic number density map. The blue lines are the corresponding subdomain boundaries determined by the present method. The most typical difference between the two are the subdomain borders inside the grains due to excess local minima; a few examples have been highlighted in green. These are not a major issue as long as the subdomains are merged appropriately. Minor differences in grain boundary delineation, highlighted in cyan, are another fairly typical and rather unimportant feature. Our numerical method misses some boundaries proposed by K.R.E., highlighted in orange, but these most often correspond to grain boundaries whose existence is somewhat ambiguous.

We compared the method to a previous atom-based method from Ref. [13]. The previous method is applicable to hexagonal lattices and has been shown to be robust and highly accurate. Figure 5 offers a comparison between the grains and the subdomains given respectively by the previous (red) and the present method (blue). The overall agreement between the two methods is very good and most deviations involve minor differences in grain delineation and small potential artifacts due to ambiguous grain boundaries and individual dislocations creeping close to grain boundaries; some examples are highlighted within the green circle. There is a handful of more complicated structures, circled in orange, where the present method may misplace or miss ambiguous grain boundaries. As discussed in Ref. [13], such boundaries are very difficult to recover in a robust fashion, either with manual or numerical segmentations. Ultimately, such problems concern only about 1% of all the grains in the system.

2. Assessment and optimization of subdomain merging

The final grain structures obtained from the subdomain merging step were benchmarked and optimized against hand segmentations of grain network images. The hand segmentations were generated by first plotting the subdomains given by the method. Authors P.H., K.R.E., and G.M.L.B. then used image manipulation software to recolor the subdomains, using (non)identical colors for two neighboring subdomains to indicate that they should (not) be merged. The manipulated images were loaded into the grain extraction program and the code merged the subdomains accordingly for further analysis.

For each lattice type, multiple systems at different time steps and with different average grain sizes were considered. A more comprehensive assessment was carried out for hexagonal systems for which P.H., K.R.E., and G.M.L.B. all prepared their own hand segmentations. The agreement between the segmentations of the code and those of the authors was measured by calculating the fraction of neighboring subdomain pairs that were treated, i.e., merged or not merged, similarly. The misorientation limit θ^* for the merging criterion was varied to find the optimal value for each lattice type. For the norm of the gradient $|\nabla\phi|^p$ in Eq. (4), $p = 2$ for the periodic lattices and $p = 1$ for the quasilattices appeared to increase the extraction accuracy. The exponent p influences the shape of the deformation field χ, hence also the distribution of its local minima and ultimately the subdomains grown, all in a nontrivial fashion. The values reported were discovered by trial and error.
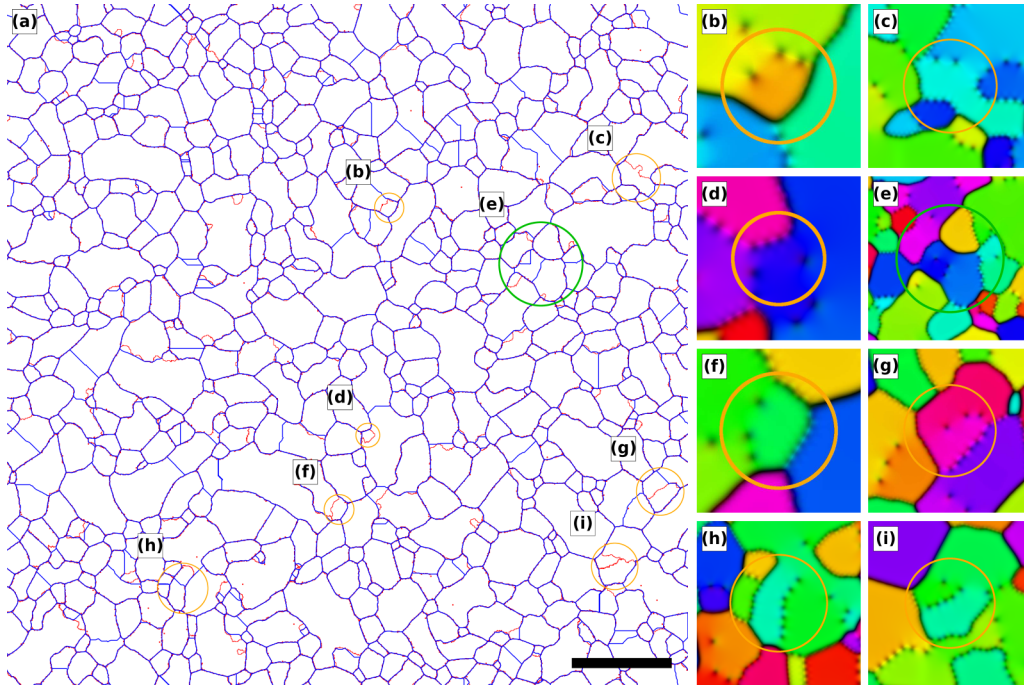
FIG. 5. (a) A comparison between the grains and subdomains produced by the previous [13] (red) and the present (blue) methods, respectively. (b)–(i) Blow-ups of the orientation field ϕ around certain structures [indicated by their respective labels in (a)]. The scale bar has length $150a_{\text{hex}}$. The blow-ups are not to scale; compare with (a). See text for details.

Figure 6(a) compares the level of agreement of the present method with the manual segmentations and with the previous atom-based method, for hexagonal systems as a function of θ^*. Note that the limit $\theta^* = 0°$ corresponds to omitting the subdomain merging step and treating each subdomain as a separate grain. The five hexagonal systems hand segmented had 622 pairs of neighboring subdomains in total and their average linear grain sizes varied from approx. 180 to approx. 590 (in dimensionless units where the approximate lattice constant is $a_{\text{hex}} = 4\pi/\sqrt{3} \approx 7.3$). The average linear grain size is given by

$$\langle d \rangle = \sqrt{S/N}, \tag{7}$$

where S is the total area of a system and N is the number of grains in it. Comparison to the previous method was carried out similarly to the hand segmentations by comparing the colors in the image files representing the numerical segmentation. The segmentations of the previous method were prepared using the fixed set of parameters found optimal in Ref. [13]. The five much larger hexagonal systems segmented in an automated fashion by the previous method had a total of 13 673 pairs of neighboring subdomains and the average linear grain sizes varied from approx. 170 to approx. 660. The values and the error bars shown are the average and standard error, respectively, of the agreements for the individual systems segmented.

Figure 6(a) shows that although the error margins are relatively large at the scale shown, the present method performs very well as compared to the hand segmentations of both P.H. and K.R.E., peaking around $\theta^* \approx 2.5°$. The agreement with G.M.L.B.'s hand segmentations appears slightly higher for $\theta^* > 3°$ and peaks around $\theta^* \approx 3.75°$. The agreement

with the previous method's segmentation is a bit lower for $\theta^* > 4°$, a bit higher for $\theta^* < 0.5°$ and peaks around $\theta^* \approx 2.75°$. Despite these minor differences, the present method's agreement with all segmentations is high and consistent for the wide, approximate range of $1° \leqslant \theta^* \leqslant 4°$. While the grain boundaries with such low misorientation are often somewhat ambiguous, all manual and the two numerical segmentations are mutually consistent. This shows that the two grain extraction methods could be substituted for the extremely tedious manual segmentation with little or no loss in accuracy. Table II summarizes the maximal agreement and the corresponding θ^* for each author.

As mentioned above, the hand segmentations have minor differences between them. The cases where there are differences in merging the subdomains are generally somewhat ambiguous and involve corners or appendages of grains where there is some change in orientation and individual dislocations are also often involved. Supplemental Fig. S3 [27] showcases some common examples.

TABLE II. Maximal level of agreement and the corresponding θ^* of the present method with the hand segmentations of P.H., K.R.E., and G.M.L.B., and with the segmentations of the previous method [13], all for hexagonal systems.

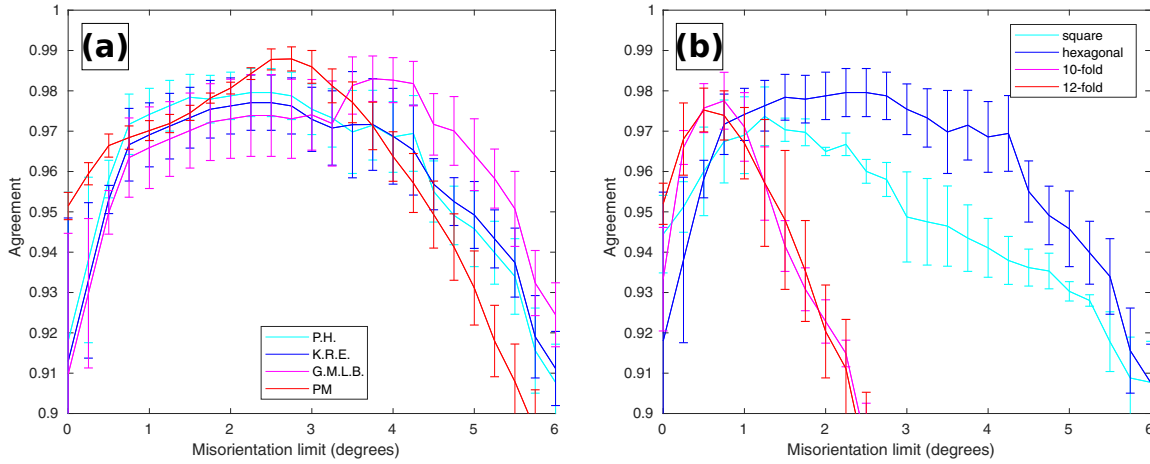| Segmentation	Agreement	θ^* (degrees)
P.H.	0.980 ± 0.006	2.5
K.R.E.	0.977 ± 0.007	2.5
G.M.L.B.	0.983 ± 0.006	3.75
Previous method	0.988 ± 0.003	2.75

FIG. 6. (a) Level of agreement (normalized to a maximum level of unity) of the present method with the hand segmentations of the authors P.H., K.R.E., and G.M.L.B., and with the segmentations of the previous method (PM) [13] for hexagonal systems, as a function of the misorientation limit θ^*. (b) Level of agreement of the present method with the hand segmentations of P.H. for square and hexagonal, as well as for ten and 12-fold quasicrystalline lattices, as a function of θ^*.

Figure 6(b) demonstrates the present method's agreement with the hand segmentations of P.H. for all four lattice types considered in this work as a function of θ^*. For the hexagonal lattice, the same data set as in Fig. 6(a) is shown, but to reiterate, the maximal level of agreement for the hexagonal lattice is 0.980 ± 0.006 at $\theta^* \approx 2.5°$. For the square lattice, the agreement is maximized at $\theta^* \approx 1.25°$ and is 0.974 ± 0.007. For the ten and 12-fold quasicrystals, the agreement is maximized at $\theta^* \approx 0.75°$ and $0.5°$, and is 0.978 ± 0.007 and 0.975 ± 0.005, respectively. Compared to the periodic lattices, the respective agreements are much more sensitive to θ^*, as the agreement falls below 0.9 already where $\theta^* \geqslant 2.5°$. Table III summarizes the maximal levels of agreement and the corresponding θ^* for each of the three other lattice types.

We would like to point out that the optimal value for θ^* need not be proportional to the order of the rotational symmetry m. The present method shows a varying tendency to produce excess subdomains for the different lattice types and, the more subdomains there are, the smaller the misorientation between them, and *vice versa*. The tendency to subdivide grains into subdomains depends on the spread of the Gaussian smoothing kernel G in Eq. (1), required to filter out the atomic-level structure, and on the exponent p in Eq. (4), which influence together the distribution of local minima in the deformation field χ.

TABLE III. Maximal level of agreement and corresponding θ^* of the present method with the hand segmentations of P.H. for square, and ten and 12-fold quasicrystalline systems. The number of neighboring subdomain pairs P and the ranges of the average linear grain sizes $\langle d \rangle$ are also given.

Lattice type	Agreement	θ^* (degrees)	P	$\langle d \rangle$
square	0.974 ± 0.007	1.25	1496	$280 - 650$
ten-fold	0.978 ± 0.007	0.75	1297	$290 - 530$
12-fold	0.975 ± 0.005	0.5	1031	$270 - 580$

3. Applicability to molecular dynamics data

Lastly, Fig. 7 demonstrates the applicability of the method to MD atomic number density data for graphene. We observed similar results for all samples and showcase here a single example. The 1 K configuration displays faint long-wavelength ripples, due to out-of-plane buckling of the monolayer, but this causes no issues. The thermal fluctuations far greater in the 300 K configuration lead to noticeable short-wavelength ripples in the corresponding orientation field, which results in a multitude of excessive subdomains. Despite this, the method is ultimately able to recover most of the grain structure. Here, $\theta^* = 2°$ was used.

At 300 K, the method ends up merging—erroneously to our opinion—the two grains at the top of the figure. At 1 K, the dumbbell-shaped composite of two subdomains at the periodic corner of the figure is treated as two separate grains as their misorientation $\theta > \theta^* = 2°$. At 300 K, the method considers the corresponding set of subdomains a single grain. Another noticeable difference between the high- and the low-temperature configurations is the delineation between the grains in lower right, but this case is a somewhat ambiguous one.

B. Microstructural analysis of different lattice types

The present grain extraction method was used to analyze the microstructure and evolution of four different lattice types. Regular periodic square and hexagonal lattices as well as ten and 12-fold quasilattices were studied to compare and to shed light on the microstructure especially in quasicrystals. Various microstructural properties were investigated, but to focus on the most relevant results and to keep this section concise, part of the results are given in detail in Supplemental Sec. S4 [27]. A brief summary of these results is given here.

All values and error bars plotted here are the mean and the standard error, respectively, of parallel realizations of model systems. Unless stated otherwise, results for the lattice types will be listed in the order of increasing m: square, hexagonal, ten-fold, and 12-fold. For the four lattice types, 16,
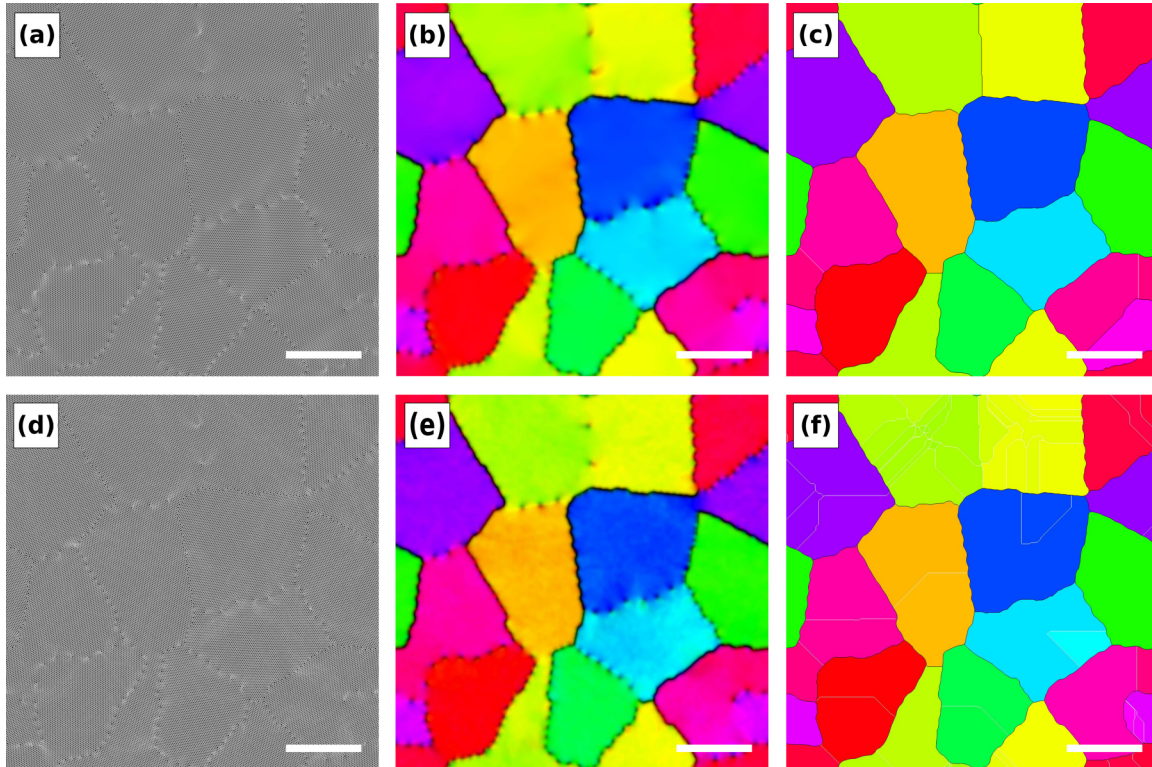
FIG. 7. Demonstration of the grain extraction method for MD data on graphene. The top (bottom) row corresponds to a system thermalized at 1 K (300 K). Panels (a) and (d) give the density field obtained by substituting small Gaussian peaks at the projected atom positions, (b) and (e) give the orientation field ϕ, and (c) and (f) give the grain structure extracted. In (c) and (f), white borders indicate that the neighboring subdomains have been merged as parts of the same grain, whereas black borders give the grain boundaries between true grains. The scale bars have an approximate length of 40 graphene lattice constants.

16, 32, and 32 parallel realizations of PFC grain coarsening simulations were conducted. All realizations had a size of 8192×8192 grid points and the spatial discretizations were $\Delta x = \Delta y = 0.55, 0.8, 0.5$, and 0.4. The systems were evolved for 5×10^6 time steps each and the time step sizes were $\Delta t = 0.5, 0.4, 0.02, 0.01$. We also compared our systems to random Voronoi tessellations in some instances. A total of 100 random seed points was sampled into each periodic Voronoi system of 4096×4096 grid points. A total of 1000 parallel realizations were generated.

1. Evolution of average linear grain size

As an archetypal benchmark of microstructural analysis, we first consider grain growth. Based on theoretical models [38–40], power-law growth is expected for the average grain size

$$\langle d(t) \rangle = \alpha(t + t_0)^\beta, \qquad (8)$$

where α, t_0 and β are fitting parameters, β known as the growth exponent. While curvature [38,39] and long-range diffusion [40]-driven growth correspond to well-defined universality classes of growth with $\beta = 1/2$ and $1/3$, respectively, PFC captures a more comprehensive picture of the microstructure, which incorporates numerous defect structures. We fitted our data of average grain sizes as a function of time with Eq. (8) to find β for the different lattice types. Note that the relaxations were initialized with rather artificial tiled states, corresponding to different nonzero grain sizes at simulation

time $t = 0$. Figure 8 gives the evolution of the average grain size for the four lattice types as a function of shifted time where the time offset t_0 due to the nonzero initial grain size
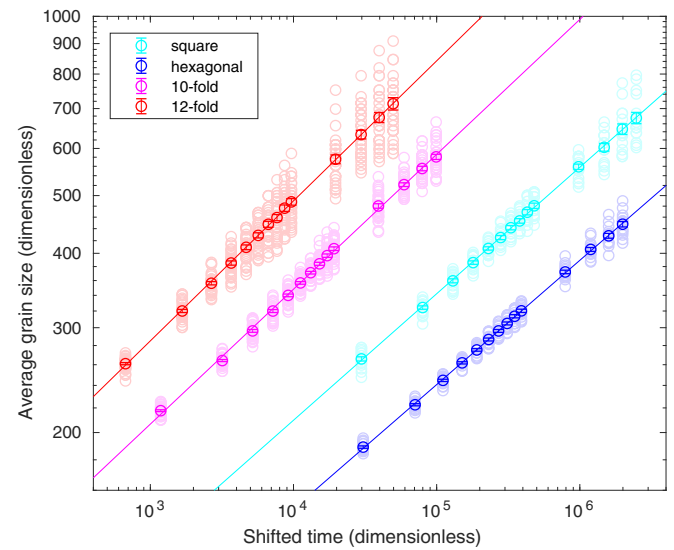

FIG. 8. Evolution of the average linear grain size averaged over the individual realizations as a function of shifted time for the four lattice types considered. See the main text for an explanation of the shifted time. The markers are actual data and the straight lines are power-law fits. The fainter ghost markers show the average linear grain sizes of individual realizations.
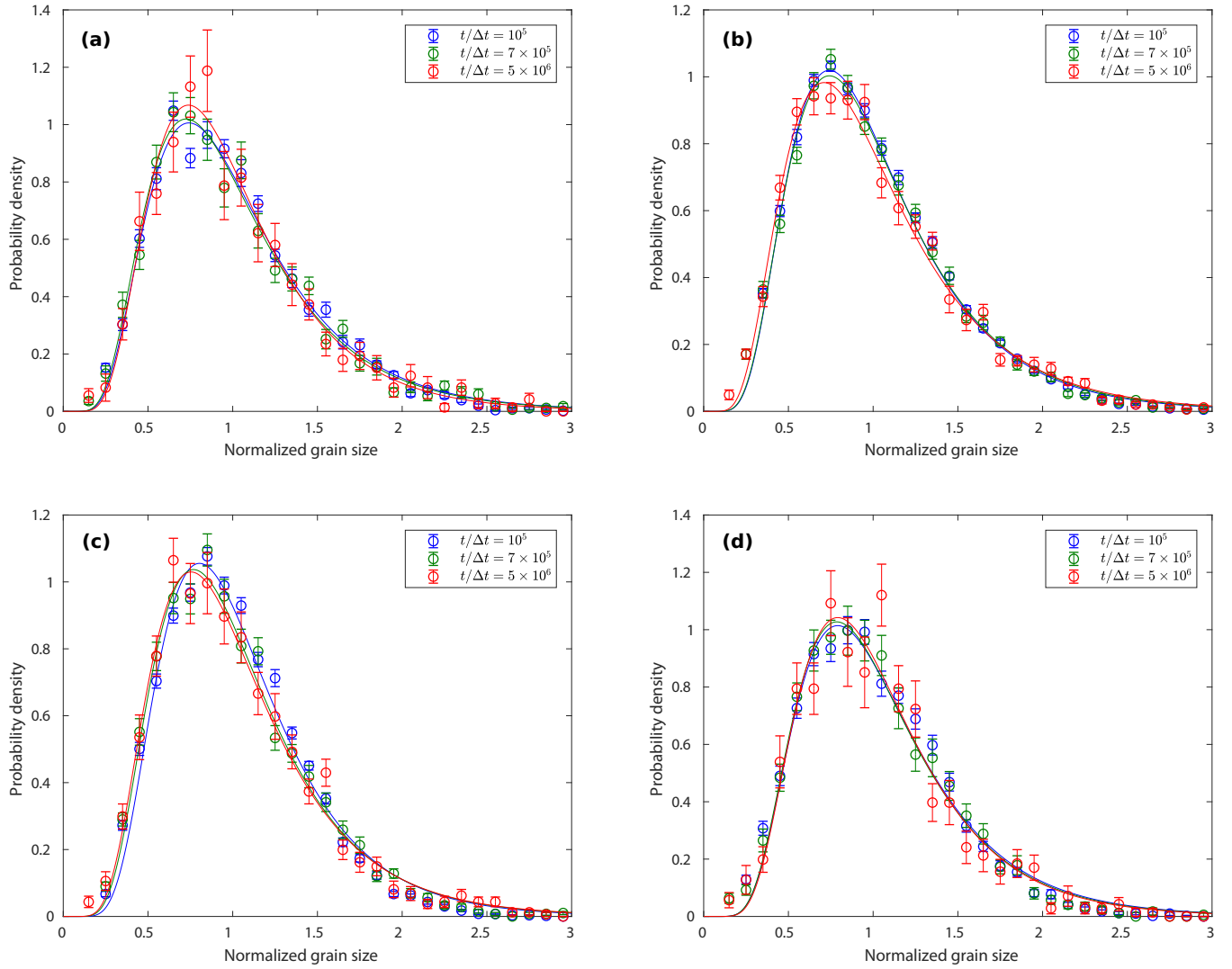
FIG. 9. Normalized grain size distributions for the four lattice types. Regular (a) square and (b) hexagonal, and (c) ten-fold and (d) 12-fold quasicrystal lattices. Three distributions are given at roughly exponentially spaced time steps. The markers are actual data and the curves are log-normal fits. The markers and error bars give the mean and the standard error, respectively, of the 16, 16, 32, and 32 parallel realizations of square, hexagonal, ten-fold and 12-fold model systems; recall the beginning of Sec. III B.

has been eliminated. Perfect power-law growth is observed for all lattice types with exponents $\beta = 0.21, 0.21, 0.23$, and 0.24. The hexagonal model used here is identical to that of Backofen *et al.* [11], and we obtain essentially the same growth exponent: our $\beta = 0.21$ vs their $\beta = 0.2$. Note that they originally reported $\beta_A = 2/5$ for grain area A, which corresponds to $\beta = 1/5$ for the linear grain size. The linear sizes of the model systems are approx. 4500, 6600, 4100, and 3300 in dimensionless units, which are much larger than the corresponding average linear grain sizes even at $t/\Delta t = 5 \times 10^6$.

2. Normalized grain size distributions

Figure 9 shows the normalized grain size distributions $d/\langle d \rangle$, where the size of an individual grain $d = \sqrt{A}$, i.e., it is taken to be the square root of the grain's area A. The distributions appear log-normal as has been reported previously [11,13,41]. A sufficient but not necessary cause for

a log-normal distribution is a proportionate growth process [42]. However, it has recently been shown that a failure to detect low-angle grain boundaries can also result in detecting a log-normal grain size distribution where the true distribution is in fact different [43]. While either or both may be the case here, the present grain extraction method was optimized to reproduce the segmentations determined by visual inspection by one of the authors (P.H.), wherein any error ultimately lies with human judgment. On the other hand, the present data cannot confirm the observation that, for a hexagonal lattice, the distributions should become wider in time [13]. There, an efficient numerical scheme [32] was used to push grain coarsening significantly further. Due to the greater computational workload, brought about by the four lattice types considered in this work, we limited ourselves to significantly shorter simulation times and can therefore neither confirm nor refute this observation. Regarding the different lattice types considered here, there are no obvious differences between them.
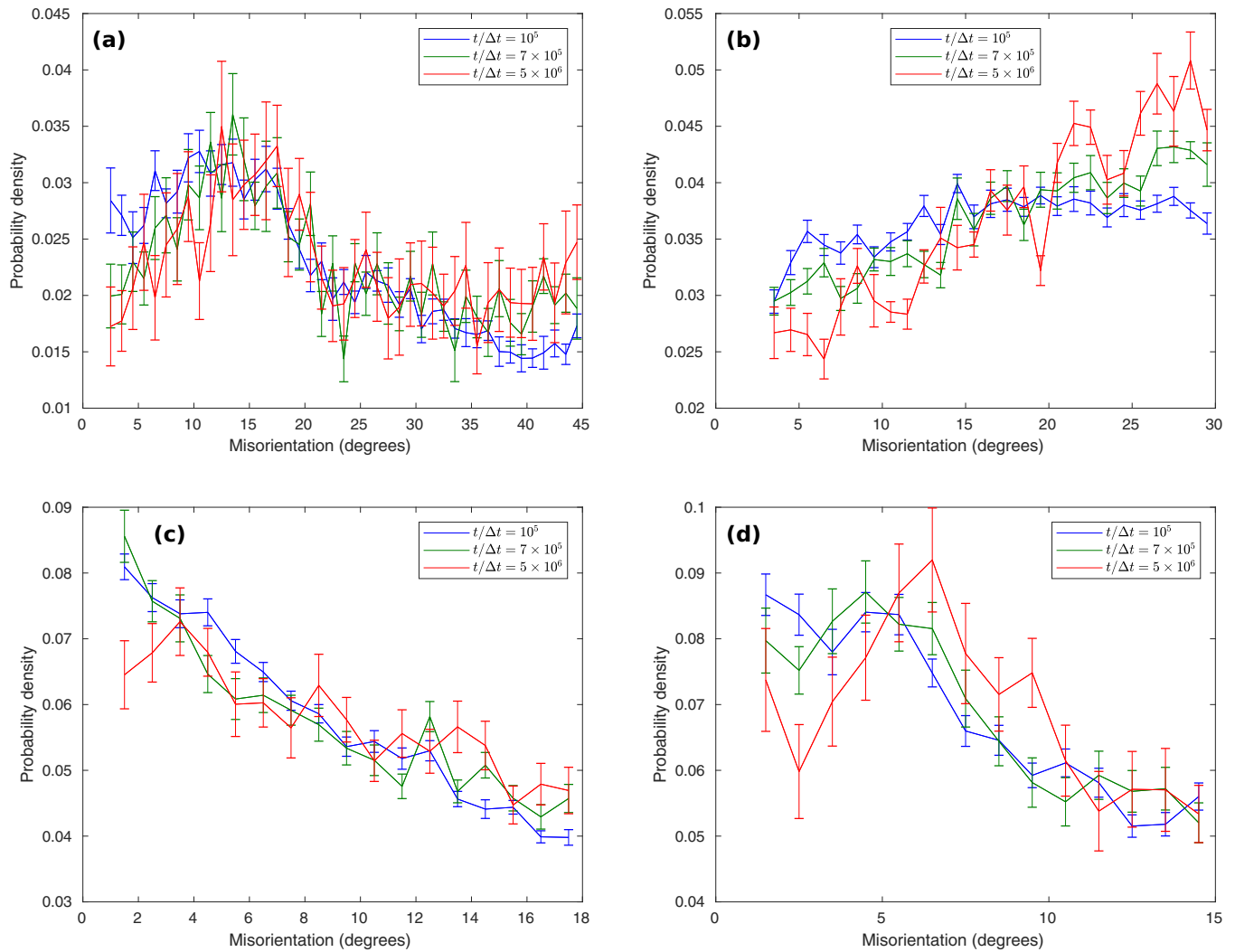
FIG. 10. Distributions of lattice misorientation between neighboring subdomains of neighboring grains for the four lattice types. Periodic (a) square and (b) hexagonal, and (c) ten-fold, and (d) 12-fold quasicrystalline lattices. Three distributions are given at roughly exponentially spaced time steps.

The late time distributions display slightly more variance and these impaired statistics are due to larger, but fewer grains in the later systems. All the PFC distributions presented in this subsection and in Supplemental Sect. S4 [27] are affected. Furthermore, the left-hand side tails are missing a couple of the leftmost data points in some cases, due to the size limit for extracting very small grains; recall Sec. II A. All bins overlapping with the limit have been omitted.

3. Grain misorientation distributions

Figure 10 shows the distributions of lattice misorientation between neighboring subdomains of neighboring grains for the four lattice types. Considering the misorientation between subdomains instead of grains (composed of, and their orientation averaged over, one or multiple subdomains) yields more accurate results. The frequencies of different misorientations have been normalized with corresponding grain boundary lengths. Note also that the maximal misorientations are $\theta = 45°$, $30°$, $18°$, and $15°$. All bins overlapping with the misorientation limits $\theta^* = 3.0, 2.5, 0.75$, and 0.5 have been omitted.

The distributions appear very dissimilar between the four lattice types. The distributions for both the hexagonal lattice and the ten-fold quasi-lattice are approximately linear, but, surprisingly, the former gives more probability for larger and the latter for smaller misorientations. On the other hand, the distributions for the square lattice and the 12-fold quasilattice are not as trivial to characterize, but both display wide excess around $\theta \approx 15°$ and $\theta \approx 7°$, respectively.

Regarding hexagonal systems, a slight preference toward smaller misorientations has previously been reported [13,41]. The present method was used to analyze different time steps of a hexagonal model system used in Ref. [13]. We confirm this conflicting preference toward smaller misorientations, whereby it appears that the misorientation distributions are dependent not only on the lattice type, but also on the model used and its parameters. This stands to reason, because the grain boundary energy—a prime driver of microstructure evolution—depends strongly on the PFC model [12] and parameters [44]. In addition, while Ref. [13] reported an excess at $\theta \approx 10°$, we do not see such a feature in our data, but, with extended simulation times, it could be possible for

TABLE IV. Summary of results of the microstructural analysis of different lattice types. Results are reported for the periodic square and hexagonal lattices as well as for the ten and 12-fold quasilattices. Results for random Voronoi tessellations are also given where applicable. Distribution types and corresponding average quantities are given where applicable. The averages are reported for $t/\Delta t = 5 \times 10^6$. The asterisks indicate that at least some of the corresponding distributions display finite size or time effects.

Average grain size	Growth exponent	
square	0.21	
hexagonal	0.21	
ten-fold	0.23	
12-fold	0.24	
Normalized grain size distributions	Type	
square	log-normal	
hexagonal	log-normal	
ten-fold	log-normal	
12-fold	log-normal	
Grain misorientation distributions	Description	
square	excess around $\theta \approx 15°$	
hexagonal	linear, larger misorientations preferred	
ten-fold	linear, smaller misorientations preferred	
12-fold	excess around $\theta \approx 7°$	
Grain size ratio distributions	Type	Average
square	nontrivial	0.62
hexagonal	nontrivial	0.61
ten-fold	nontrivial	0.64
12-fold	nontrivial	0.64
Voronoi	truncated normal	0.80
Grain aspect ratio distributions	Type	Average
square	truncated normal	0.70
hexagonal	truncated normal	0.66
ten-fold	truncated normal	0.72
12-fold	truncated normal	0.71
Voronoi	truncated normal	0.63
Grain misalignment distributions	Description	
square	smaller misalignments preferred	
hexagonal	smaller misalignments preferred	
10-fold	smaller misalignments preferred	
12-fold	smaller misalignments preferred	
Voronoi	intermediate misalignments disfavored	
Grain circularity distributions	Type	Average
square	reversed log-normal *	0.76
hexagonal	reversed log-normal	0.75
ten-fold	reversed log-normal *	0.78
12-fold	reversed log-normal *	0.77
Neighbor count distributions	Type	Average
square	log-normal	5.99
hexagonal	log-normal	6.00
ten-fold	log-normal	5.99
12-fold	log-normal	5.96

a corresponding bump to emerge. Lastly, qualitatively similar PFC models have been shown to predict energetically favored symmetrically tilted coincidence site lattice boundaries for misorientations $\theta \approx 18°$, $21°$, and $28°$ [12]. The present data do display some excess for these misorientations, but, due to the relatively large error bars, we cannot conclusively distinguish these bumps from statistical fluctuations.

For the square lattice, we carried out grain boundary energy calculations using symmetrically tilted bicrystals to investigate the possibility of a connection between the features of the grain boundary energy and the misorientation distributions. However, the grain boundary energy measured appears very smooth and virtually featureless as a function of the tilt angle, and shows no kinks that could explain the excess observed at $\theta \approx 15°$. We also investigated the grain boundary energies of symmetrically tilted grain boundaries for 12-fold quasicrystals, but again the energies obtained show no hints of particularly low-energy boundaries around $\theta \approx$

$7°$. We must point out, however, that our analysis was not exhaustive and may have failed to detect hypothetical narrow kinks in grain boundary energy. In fact, unpublished results of author CVA show evidence of a possibly related kink at $\theta \approx 5.5°$, which is in agreement with the interface dynamics when growing quasi-crystals from two seeds of different size [24]. Full details of the grain boundary energy calculations are given in Supplemental Sec. S5 [27]. More comprehensive investigation of quasicrystal grain boundary energies will be left for a future work. Before concluding on grain boundary energies, we would like to point out that the present grain extraction method does not distinguish between symmetric and asymmetric tilt boundaries of identical misorientation, and that the former are a special case of grain boundaries whereas the latter more general family of grain boundaries is much more abundant in the present microstructures. Unfortunately, investigating grain boundary energies with the additional degree of freedom brought about by asymmetric boundaries goes well beyond the scope of this work.

4. Summary of additional results

The rest of the microstructural results are given in full detail in Supplemental Sec. S4 [27]. Table IV lists all main results from this section. The grain size ratios, the ratios of linear sizes between neighboring grains, were observed to have averages 0.62, 0.61, 0.64, and 0.64 (at $t/\Delta t = 5 \times 10^6$), meaning that some disparity is preferred. This is in contrast to random Voronoi tessellations with a different distribution and an average of 0.80. However, the corresponding area ratios were found to be in excellent agreement with the PFC distributions of Ref. [13]. The grain aspect ratios, i.e., the ratio of the shorter principal axis to the longer, were found to be modest with averages 0.70, 0.66, 0.72, and 0.71 (at $t/\Delta t = 5 \times 10^6$), meaning that the most grains are slightly elongated. This is in reasonable agreement with random Voronoi tessellations with an average of 0.63. The aspect ratios are normally distributed. The grain misalignment, or the angle between the longer principal axes of two neighboring grains, shows tendency toward mutual alignment. In contrast, random Voronoi tessellations disfavor intermediate misalignments. We ascribe this difference to PFC's ability to capture the interactions and anisotropy of grain boundaries [12,45]. We observed reversed log-normal grain circularities

$$C = \frac{4\pi A}{P^2}, \tag{9}$$

where A is grain area and P its perimeter, for all lattice types. The average circularities are 0.76, 0.75, 0.78, and 0.77 (at $t/\Delta t = 5 \times 10^6$), all slightly less circular than a square [46] due to grain elongation. All other lattice types except hexagonal show some finite size effects or vestiges of the artificial, tiled initial state as the distributions start off as not quite log-normal. It is surprising that, while all distributions for all other quantities at $t/\Delta t = 10^5$ have converged to their respective equilibrium shapes, the relaxation timescale for circularities can be longer. Distributions for the number of neighbors per grain are also log-normal with averages 5.99, 6.00, 5.99, and 5.96. More or less similar values have been reported for random Voronoi tessellations (6)

[47], PFC systems (6.0) [13] and experimental systems (5.8) [41].

IV. SUMMARY AND CONCLUSIONS

In this paper, we have introduced and comprehensively benchmarked an efficient and accurate method for extracting grains and analyzing the microstructure in 2D poly and quasicrystalline solids. The present method was optimized for different periodic and quasilattices based on manual segmentations. A high level of agreement was achieved in all cases. We expect that the accuracy of the method could be further improved by utilizing machine learning techniques for the final subdomain merging step of the method. We also showed that the present method is applicable to MD-generated data of free-standing graphene. It should also be possible to modify the method to segment diffuse microstructures from phase field simulations. Generalizing this method to 3D lattices and quasilattices would be more complicated, but also extremely valuable. The main obstacle is forming the orientation field for a 3D system; the other steps of the algorithm would remain essentially the same. Due to the large domains and long timescales required in 3D, PFC is again an ideal choice for modeling them.

We used the method to analyze the microstructures of various lattice types. We considered both regular periodic square and hexagonal lattices, as well as ten and 12-fold symmetric quasicrystals. We studied the sizes, aspect ratios, circularities, and neighbor counts of individual grains; also the size ratios, misorientations and misalignments between all pairs of neighboring grains. For the most part, we observed good agreement with previous works for the hexagonal lattice, and also very similar behavior between all four lattice types, suggesting that many microstructural properties are universal beyond lattice symmetry.

However, a particularly interesting case is that of lattice misorientation between neighboring grains. A previous work reported a slight preference toward smaller misorientations for hexagonal lattices, but we observed a preference toward larger misorientations. This issue was resolved by analyzing model systems used in the previous work – we found the same preference toward smaller misorientations. This suggests that the distribution of misorientations is sensitive not only to the lattice type, but also to the exact model and its parameters being used. For square lattice and 12-fold quasicrystal, an excess of boundaries is observed with a misorientation of $\theta \approx 15°$ and $\theta \approx 7°$, respectively. We sought an explanation from grain boundary energy calculations and ruled out wide kinks in grain boundary energy as culprits of the excesses observed.

We expect the present work to be valuable in the study of both regular periodic crystals and quasicrystals. While PFC has been used successfully in the past to study quasicrystals, we have here demonstrated large-scale coarsening simulations of polyquasicrystalline microstructures. We have also presented a powerful method for analyzing those microstructures.

[1] W. D. Callister and D. G. Rethwisch, *Materials Science and Engineering: An Introduction*, 8th ed. (John Wiley and Sons, Hoboken, New Jersey, 2009).

[2] D. Hull and D. J. Bacon, *Introduction to Dislocations* (Butterworth-Heinemann, Oxford, UK, 2001).

[3] R. Grantab, V. B. Shenoy, and R. S. Ruoff, Science **330**, 946 (2010).

[4] Z. Fan, P. Hirvonen, L. F. C. Pereira, M. M. Ervasti, K. R. Elder, D. Donadio, A. Harju, and T. Ala-Nissila, Nano Lett. **17**, 5919 (2017).

[5] K. Azizi, P. Hirvonen, Z. Fan, A. Harju, K. R. Elder, T. Ala-Nissila, and S. M. V. Allaei, Carbon **125**, 384 (2017).

[6] G. J. Snyder and E. S. Toberer, Nat. Mater. **7**, 105 (2008).

[7] O. V. Yazyev and S. G. Louie, Nat. Mater. **9**, 806 (2010).

[8] S. T. Pantelides, Y. Puzyrev, L. Tsetseris, and B. Wang, MRS Bull. **37**, 1187 (2012).

[9] A. H. King, Interface Sci. **7**, 251 (1999).

[10] Y. Mishin, A. Suzuki, B. P. Uberuaga, and A. F. Voter, Phys. Rev. B **75**, 224101 (2007).

[11] R. Backofen, K. Barmak, K. Elder, and A. Voigt, Acta Mater. **64**, 72 (2014).

[12] P. Hirvonen, M. M. Ervasti, Z. Fan, M. Jalalvand, M. Seymour, S. M. Vaez Allaei, N. Provatas, A. Harju, K. R. Elder, and T. Ala-Nissila, Phys. Rev. B **94**, 035414 (2016).

[13] G. Martine La Boissonière and R. Choksi, Modell. Simul. Mater. Sci. Eng. **26**, 035001 (2018).

[14] H. M. Singer and I. Singer, Phys. Rev. E **74**, 031103 (2006).

[15] B. Berkels, A. Rätz, M. Rumpf, and A. Voigt, J. Sci. Comput. **35**, 1 (2008).

[16] M. Elsey and B. Wirth, Multiscale Model. Simul. **12**, 1 (2014).

[17] H. Yang, J. Lu, and L. Ying, Multiscale Model. Simul. **13**, 1542 (2015).

[18] A. Stukowski, Modell. Simul. Mater. Sci. Eng. **18**, 015012 (2010).

[19] J. F. Panzarino and T. J. Rupert, JOM **66**, 417 (2014).

[20] P. A. Thiel, Annu. Rev. Phys. Chem. **59**, 129 (2008).

[21] R. McGrath, J. Ledieu, E. J. Cox, and R. D. Diehl, J. Phys.: Condens. Matter **14**, R119 (2002).

[22] J. A. Smerdon, H. R. Sharma, J. Ledieu, and R. McGrath, J. Phys.: Condens. Matter **20**, 314005 (2008).

[23] C. V. Achim, M. Schmiedeberg, and H. Löwen, Phys. Rev. Lett. **112**, 255501 (2014).

[24] M. Schmiedeberg, C. V. Achim, J. Hielscher, S. C. Kapfer, and H. Löwen, Phys. Rev. E **96**, 012602 (2017).

[25] J. Rottler, M. Greenwood, and B. Ziebarth, J. Phys.: Condens. Matter **24**, 135002 (2012).

[26] P. Subramanian, A. J. Archer, E. Knobloch, and A. M. Rucklidge, Phys. Rev. Lett. **117**, 075501 (2016).

[27] See Supplemental Material at http://link.aps.org/supplemental/10.1103/PhysRevMaterials.2.103603 for more details of our methods and additional results.

[28] K. R. Elder, M. Katakowski, M. Haataja, and M. Grant, Phys. Rev. Lett. **88**, 245701 (2002).

[29] K. R. Elder and M. Grant, Phys. Rev. E **70**, 051605 (2004).

[30] N. Provatas and K. Elder, *Phase-Field Methods in Materials Science and Engineering* (Wiley-VCH, Weinheim, Germany, 2010).

[31] K.-A. Wu, A. Adland, and A. Karma, Phys. Rev. E **81**, 061601 (2010).

[32] M. Elsey and B. Wirth, ESAIM: Math. Modell. Numer. Anal. **47**, 1413 (2013).

[33] M. Cheng and J. A. Warren, J. Comput. Phys. **227**, 6241 (2008).

[34] Z. Fan, W. Chen, V. Vierimaa, and A. Harju, Comput. Phys. Commun. **218**, 10 (2017).

[35] Z. Fan, GitHub - brucefan1983/GPUMD: Graphics Processing Units Molecular Dynamics, Doi: 10.5281/zenodo.1321311.

[36] J. Tersoff, Phys. Rev. B **39**, 5566 (1989).

[37] L. Lindsay and D. A. Broido, Phys. Rev. B **81**, 205441 (2010).

[38] J. E. Burke, AIME Trans. **180**, 73 (1949).

[39] J. Burke and D. Turnbull, Prog. Met. Phys. **3**, 220 (1952).

[40] J. Krzanowski and S. Allen, Acta Metall. **34**, 1035 (1986).

[41] K. Barmak, E. Eggeling, D. Kinderlehrer, R. Sharp, S. Ta'asan, A. Rollett, and K. Coffey, Prog. Mater. Sci. **58**, 987 (2013).

[42] J. Sutton, J. Econ. Literature **35**, 40 (1997).

[43] B. Korbuly, T. Pusztai, H. Henry, M. Plapp, M. Apel, and L. Gránásy, Phys. Rev. E **95**, 053303 (2017).

[44] M. Salvalaglio, R. Backofen, A. Voigt, and K. R. Elder, Phys. Rev. E **96**, 023301 (2017).

[45] P. Hirvonen, Z. Fan, M. M. Ervasti, A. Harju, K. R. Elder, and T. Ala-Nissila, Sci. Rep. **7**, 4754 (2017).

[46] M. M. Conroy, A table of isoperimetric ratios, (2017), https://sites.math.washington.edu/~conroy/isoperimetrics/isoperimetrics.pdf.

[47] A. Okabe, B. Boots, K. Sugihara, and S. N. Chiu, *Spatial Tessellations: Concepts and Applications of Voronoi Diagrams*, 2nd ed. (John Wiley, Chichester, West Sussex, 2000).